# Reconfigurable anisotropy and functional transformations with VO₂-based metamaterial electric circuits

Salvatore Savo,[1,*] You Zhou,[2] Giuseppe Castaldi,[3] Massimo Moccia,[3] Vincenzo Galdi,[3] Shriram Ramanathan,[2] and Yuki Sato[1,†]

[1]*Rowland Institute at Harvard, Harvard University, Cambridge Massachusetts 02142, USA*
[2]*Harvard School of Engineering and Applied Sciences, Harvard University, Cambridge Massachusetts 02138, USA*
[3]*Department of Engineering, University of Sannio, I-82100 Benevento, Italy*
(Received 2 June 2014; revised manuscript received 13 March 2015; published 16 April 2015)

We demonstrate an innovative multifunctional artificial material that combines exotic metamaterial properties and the environmentally responsive nature of phase-change media. The tunable metamaterial is designed with the aid of two interwoven coordinate-transformation equations and implemented with a network of thin-film resistors and vanadium dioxide (VO₂). The strong temperature dependence of VO₂ electrical conductivity results in a significant modification of the resistor network behavior, and we provide experimental evidence for a reconfigurable metamaterial electric circuit that not only mimics a continuous medium, but is also capable of responding to thermal stimulation through dynamic variation of its spatial anisotropy. Upon external temperature change, the overall effective functionality of the material switches between a "truncated cloak" and a "concentrator" for electric currents. Possible applications may include adaptive matching resistor networks, multifunctional electronic devices, and equivalent artificial materials in the magnetic domain. Additionally, the proposed technology could also be relevant for thermal management of integrated circuits.

## I. INTRODUCTION

Materials synthesis has reached a point where one can literally grow materials from scratch while manipulating the substance at the atomic and molecular level. This has led to various new possibilities for material properties that never existed in the past. A related field that has also seen a tremendous growth in recent years is metamaterial engineering. Artificial structures from nanoscales and up can be fabricated to collectively induce exotic properties not typically found in nature. Traditionally proposed as a platform for studying electromagnetic phenomena, metamaterials have expanded beyond the realm of optics [1,2], and have seen applications in diverse areas including the manipulation of acoustic waves [3–5], magnetostatic fields [6–8], heat flux [9–11], and electric currents [12].

In the area where the fields of material science and metamaterial engineering overlap, the ability to reconfigure the response of the materials in real time has emerged as one of the most important goals. For electromagnetic waves, the hybrid-metamaterial approach has been successful. For instance, metastructures with graphene [13], chalcogenide glass [14], liquid crystals [15], nano- and micromechanical switches [16], superconductors [17], and vanadium dioxide (VO₂) [18,19] have resulted in linear and nonlinear control of transmission characteristics, yielding frequency tunability. In contrast to these time-varying counterparts, however, the incorporation of similar hybridized structures in static (or quasistatic) electric and magnetic metamaterials has been largely unexplored to date. Unlike the above resonant metamaterials, where reconfigurability has traditionally been used to shift their frequency response, (direct current) dc hybrid metamaterials are more feasible for great operational shift.

In this paper, we report the experimental integration of VO₂ phase-change materials in dc electric metamaterial structures.

We have designed a metamaterial electric circuit (MMEC) with cloakinglike and concentratinglike functionalities with the aid of a coordinate-transformation-based approach [20]. We then implemented the MMEC on a 4-in. silicon wafer using thin-film technology and circuit theory. The material switches by itself from one functionality to the other via VO₂ metal-to-insulator phase transitions induced by an external temperature change. The experimental results and the theoretical approach presented here may pave the way to analogous investigations and potential applications in a multitude of electrical, magnetic, and thermal systems.

Accordingly, the rest of the paper is organized as follows. In Sec. II, we outline the problem statement and the general approach. In Sec. III, we illustrate the design and parameters and present and discuss the numerical and experimental results. Some brief concluding remarks follow in Sec. IV, with technical details relegated to three Appendixes.

## II. PROBLEM STATEMENT AND APPROACH

In tailoring the spatial anisotropy of dc metamaterials, previous works have focused on single functionalities (e.g., cloak or concentrator) [12,21,22], or have made use of additional dc sources for altering the spatial distribution of electric currents [23]. For realistic applications, the ability of a metamaterial electric (and, eventually, electronic) circuit to readily respond to the surrounding environmental variations (e.g., temperature changes) is of strategic importance. Combining metamaterials with environmentally responsive material compounds could pave the way for such multifunctional MMECs.

We begin by introducing the ideal model of the metamaterial system under study. Figure 1(a) illustrates a homogeneous, isotropic material background of conductivity $\sigma_0 = 600$ S/m (blue-color-coded area) enclosed in a circular domain of radius $R_0 = 40$ mm, with an annular region of radii $a$ and $b$ (orange-color-coded area) filled with an inhomogeneous, anisotropic "transformation medium" of (tensor) conductivity $\bar{\bar{\sigma}}$. The multifunctional scenario considered here naturally requires
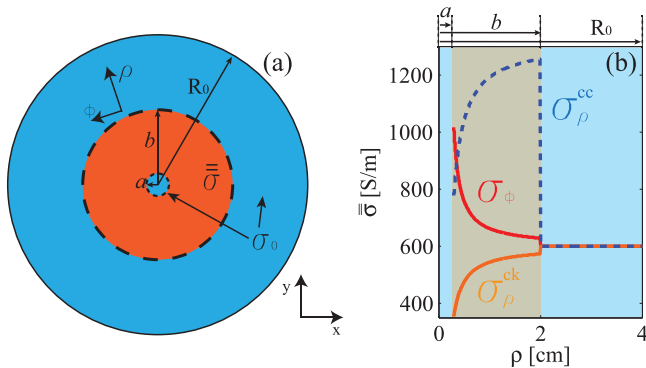
*savo@rowland.harvard.edu
†sato@rowland.harvard.edu

FIG. 1. (Color online) (a) Color-coded 2D model of the ideal MMEC. Blue regions indicate a homogeneous, isotropic material with conductivity $\sigma_0 = 600$ S/m, whereas orange color indicates the transformation-medium region with inhomogeneous, anisotropic conductivity. (b) Conductivity profiles derived via the coordinate-transformation framework (see Appendix A).

two different spatial profiles for the electrical conductivity with a way to switch between the two. To demonstrate reconfigurability, we have selected the examples of cloakinglike and concentratorlike functionalities. We refer to the coordinate-transformation framework to determine the conductivity profiles pertaining to the two scenarios [see Fig. 1(b)]. Such coordinate-transformation-based designs have the exclusive advantage of being naturally impedance matched [20,24,25], and for this reason the load variation arising from spatial resistance change would (ideally) not be sensed by the external circuitry and sources.

Next, we view the ideal material as a system consisting of an ensemble of elements that collectively give rise to the material's overall characteristics. This conceptual transition from a continuous medium to an equivalent discretized version provides a powerful tool for designing the anisotropic properties of artificial materials and introduces a functional component better suited for practical implementations [12,21–23,26]. In this particular case, we mimic a continuous, anisotropic, cylindrical conducting medium of conductivity $\bar{\bar{\sigma}}$ and thickness $t$ by means of a polar resistor network comprising of spokes and arcs of finite lengths, whose dimensions can be calculated from Ohm's law:

$$R_\rho = \frac{\Delta\rho}{t\sigma_\rho\rho\Delta\phi}, \quad R_\phi = \frac{\rho\Delta\phi}{t\sigma_\phi\Delta\rho}, \tag{1}$$

where $\Delta\rho$ and $\Delta\phi$ are the radial and angular dimensions of the MMEC unit cell, respectively, with $\rho$ and $\phi$ denoting the radial and angular directions, respectively, in cylindrical coordinates.

Figure 2(a) shows a color-coded model of the geometry of the MMEC polar networks where each color refers to a different material. By properly assigning the dimensions and conductivities of the polar grid elements, it is possible to mimic the properties of any continuous medium and hence achieve unprecedented control over the electric current flowing through the material. The material discretization is followed by the assignment of resistance values for all constitutive elements. Figure 2(b) illustrates the corresponding resistance profiles calculated via Ohm's law using the conductivities values shown in Fig. 1(b). Moreover, we employ VO$_2$ as
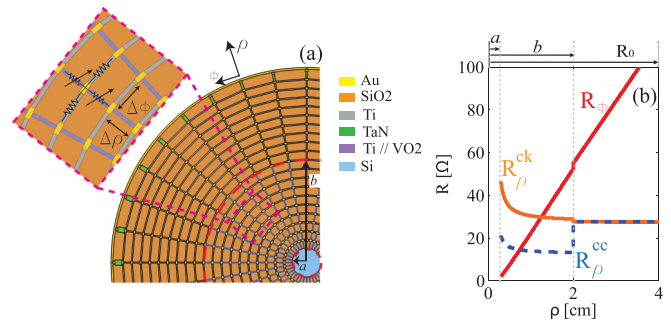


FIG. 2. (Color online) (a) Color-coded COMSOL model used for the simulation of the MMEC response. The inset shows a closeup of the tunable region where thin-film resistors are modeled with rectangular elements oriented in the radial (variable resistor symbol) and angular (fixed resistor symbol) directions. The anisotropic properties are changed by varying the resistivity of the purple elements. (b) Resistance values derived from coordinate-transformation equations [cf. (1)] used to calculate the dimensions of the Ti and VO$_2$ thin-film resistors in the radial and angular directions $R_\rho^{ck}$, $R_\rho^{cc}$, and $R_\phi$.

a temperature-dependent switch to implement the transition between the two functionalities. Extension of the polar resistor network in the homogeneous and isotropic core region was extremely challenging from the fabrication point of view. For this reason, we used a silicon wafer ($\sigma = 10$ S/m) to fill the core area, as this material provides a mechanical support for the MMEC and is compatible with the microfabrication process used to build the device. Furthermore, the numerical simulation results presented in Sec. III confirm that the conductivity mismatch introduced by the silicon core does not sensibly affect the performance of the device.

It is worth mentioning that the proposed resistive network topology itself is relevant for many circuit applications including filters [27,28], matching networks for power electronics [29], and electric impedance tomography [30,31]. Design strategies include minimization of power dissipation [32] and resistance distance [33], and dealing with inverse problems [30]. The choice strongly depends on the desired application. In this work, we apply the resistive network to mimic a continuous medium while gaining control over the spatial anisotropy.

## III. RESULTS

### A. Design

Referring the reader to Appendix A for the details of the coordinate-transformation formalism, we limit ourselves here to reporting the two transformations that implement the desired functionalities. For the first type of anisotropic material, we induce the so-called "truncated cloak," via a well-established [34] coordinate transformation

$$f_{ck}(\rho) = \frac{b(\rho - a + \delta)}{b - a + \delta}, \tag{2}$$

which, for a vanishing truncation parameter ($\delta \to 0$), essentially compresses the space from a cylindrical region of radius $b$ into an annular region $a < \rho < b$. Thus, as $\delta \to 0$, the electrical current will be completely removed from the core region $\rho < a$.

For the second type of anisotropy, we induce a "concentrator" behavior. In this case, instead of standard coordinate transformations used in the past [21], we introduce a different transformation

$$f_{cc}(\rho) = b \left[ \frac{f_{ck}(\rho)}{b} \right]^{\gamma}, \quad 0 < \gamma < 1. \quad (3)$$

This formalism effectively links the two transformations, and makes the practical design for multifunctionality more feasible (see Appendix A for more details). Figure 1(b) shows the radial and angular components of the polar network resistance, $R_\rho$ and $R_\phi$, obtained from the coordinate-transformation framework above for the two functionalities.

In particular, we follow a simplified approach by assuming

$$R_\phi^{(ck)}(\rho) = R_\phi^{(cc)}(\rho), \quad (4)$$

so that only the radial resistance profile $R_\rho(\rho)$ needs to be reconfigured. When $R_\rho = R_\rho^{ck}$ (orange continuous curve), the overall material mimicked by the resistor grid functions as a truncated cloak. We note that a perfect cloak would require an infinite azimuthal conductivity at the core boundary, making it prohibitive to simultaneously implement the anisotropy required for the concentrating behavior. For this reason, we consider a finite truncation parameter $\delta$, which yields an *imperfect* cloaking effect, with the electrical current density inside the inner region $\rho < a$ not exactly vanishing, but reduced by a factor

$$\chi_{ck} = \frac{b}{a} \left( \frac{\delta}{b - a + \delta} \right). \quad (5)$$

On the other hand, when $R_\rho = R_\rho^{cc}$ (blue dashed curve), the current is forced to flow into the core region $\rho < a$, and can be enhanced by a factor

$$\chi_{cc} = \frac{f_{cc}(a)}{a} = \frac{b}{a} \left( \frac{\delta}{b - a + \delta} \right)^{\gamma} > 1, \quad (6)$$

where the parameter $\gamma$ needs to be suitably chosen for the inequality to hold. In fact, it is evident from (6) that in the limit $\gamma \to 1$ the imperfect cloaking functionality is attained in this case too. The parameters $\delta$ and $\gamma$ can be computed from (5) and (6), once the desired cloaking and concentration factors $\chi_{ck}$ and $\chi_{cc}$, as well as the shell dimensions $a$ and $b$, have been set. In our design, also on the basis of extensive parametric studies (see Appendix B), we chose $\chi_{ck} = 0.7$ and $\chi_{cc} = 1.5$ as a reasonable tradeoff between the two functionalities. Moreover, for the shell size, we chose $a = 3$ mm and $b = 21.5$ mm, which yields $\delta = 2$ mm and $\gamma = 0.672$.

It is worth pointing out that in our simplified scenario, where reconfigurability is achieved by changing the resistance along a single direction only (as opposed to changing both $R_\rho$ and $R_\phi$ at the same time), perfect impedance matching cannot be attained (see Appendix A for details).

### B. Fabrication and parameters

Figure 3(a) shows a camera image of our MMEC prototype fabricated on a 4-in. silicon wafer. The resistance profiles $R_\rho^{ck}$ and $R_\phi$ are implemented by patterning titanium (Ti, $\rho_{Ti} = 132 \, \mu\Omega$ cm) rectangles with fixed length (1850 $\mu$m) and thickness (200 nm) and variable width to match the desired
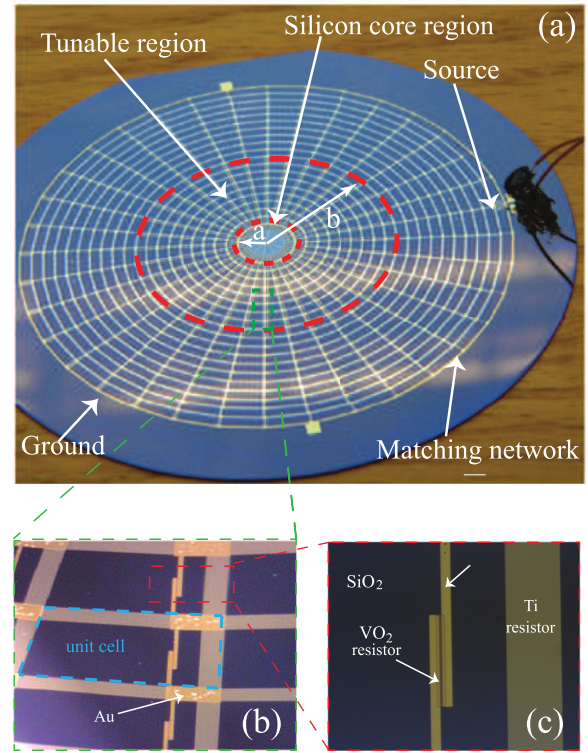


FIG. 3. (Color online) (a) Camera image of the MMEC fabricated on a silicon wafer. The area between the red dashed circles is the tunable region. $a = 3$ mm and $b = 21.5$ mm are the dimensions of the core region and tunable regions, respectively. (b) Closeup of the MMEC unit cell. (c) Closeup of the VO$_2$/Au and Ti resistors. They are both deposited on a 100 nm thermally grown SiO$_2$ layer (dark background region).

resistance values at particular locations. To reconfigure the anisotropy of the overall material mimicked by the network, VO$_2$ thin-film resistors are grown in parallel with the Ti resistors oriented radially. The three orders of magnitude reduction in the VO$_2$ electric resistivity across the phase transition allows us to approximately match the lower radial resistance required in the $R_\rho^{cc}$ profile. Figures 3(b) and 3(c) show closeups of the MMEC unit cells and the thin-film patterns, respectively. Electrical links between resistors are guaranteed by rectangular Au pads positioned at every node.

The center of the grid is left open and is electrically connected to the silicon wafer forming a core region with radius $a = 3$ mm and thickness $t = 500 \, \mu$m. The rest of the silicon wafer surface is made insulating with a layer of silicon dioxide. The core is surrounded by a tunable area of external radius $b = 21.5$ mm, in which the dimensions, and hence resistances, of all the thin-film elements on SiO$_2$ are obtained through coordinate transformations. The conductivity of the silicon core is $\sigma = 10$ S/m, and its thickness is taken into account to appropriately impedance-match it. Moreover, the outermost circle (of radius 40 mm) acts as the ground and it is connected to the rest of the circuit through matching resistors made of tantalum nitride (TaN, $\rho_{TaN} = 2280 \, \mu\Omega$ cm) to emulate an infinite material. Overall, the network consists of a 20 × 36 polar array of thin-film resistors and a 10 × 36 array of VO$_2$ elements. Details of the fabrication and growth steps

and of the calculations regarding the thin films and matching resistors, dimensions, and resistances of Au, Ti, TaNi, and VO$_2$ films can be found in Appendixes C and D, respectively.

### C. Numerical modeling

We start by illustrating the numerical modeling of the structure, carried out via finite-element numerical simulations with the commercial software package COMSOL MULTIPHYSICS [35]. The reader can refer to Appendix D for the electric conductivity values utilized in the model.

The color-coded schematics in Fig. 2(a) shows a 90° angular sector of the 2D model implemented to simulate the MMEC, where each color refers to a different material. In addition, for each unit cell inside the tunable region, we model the Ti and VO$_2$ resistor pairs with equivalent single resistors [see the purple elements in Fig. 2(a)]. The transition from $R_\rho^{ck}$ to $R_\rho^{cc}$ is obtained by changing the conductivity of the purple elements located inside the tunable region, enclosed between the two concentric red dashed circles [see the inset in Fig. 2(a)]. The conductivity of the tunable elements is varied by a factor consistent with the overall resistance change featured by the parallel resistance formed by Ti and VO$_2$ when this latter changes phase. The simulated voltage contour maps of the two functionalities, the truncated cloak and concentrator, are plotted in Figs. 4(a) and 4(b), respectively, assuming a 5 V dc bias applied to the second to the last circle [see Fig. 4(a)]. As anticipated, our choice of the geometry ($a = 3$ mm, $b = 21.5$ mm) and design ($\chi_{ck} = 0.7$, $\chi_{cc} = 1.5$) result in $\delta = 2$ mm and $\gamma = 0.672$.

An initial qualitative assessment shows a clear ability of the simulated device to switch between two distinct functionalities. Even though our design does not ensure perfect impedance matching, it is worth pointing out that the equipotential lines in

the portion of the device outside the tunable region experience negligible perturbation, whereas inside the tunable region the distribution of equipotential lines drastically changes in accordance with the coordinate-transformation equations (2) and (3). Furthermore, the variation of the anisotropy of the MMEC results in a noticeable difference in the number of voltage contour lines inside the core region in the two states (truncated cloak and concentrator).

In order to quantitatively assess the ability of the MMEC device to effectively work as a truncated cloak and a concentrator, as predicted by the $\chi_{ck}$ and $\chi_{cc}$, we compared the numerical results in Figs. 4(a) and 4(b) with a reference case. The metamaterial reference is implemented with the same polar network except for the resistors in the tunable region which feature the same constant resistance values as in the outermost region, resulting in a constant $R_\rho(\rho)$ profile and a linear $R_\phi(\rho)$ profile. The contour map of the reference simulated voltage distribution is plotted in Fig. 4(c). From these data, we can numerically estimate the cloak and concentration factors as the simulated voltage difference measured across the core region in the truncated-cloak ($\Delta V_{ck}$) and concentrator ($\Delta V_{cc}$) scenarios, respectively, divided by the counterpart value observed in the reference case ($\Delta V_{ref}$). We obtain

$$\chi_{ck}^{sim} = \frac{\Delta V_{ck}}{\Delta V_{ref}} = 0.7, \quad \chi_{cc}^{sim} = \frac{\Delta V_{cc}}{\Delta V_{ref}} = 1.9. \quad (7)$$

This confirms that the MMEC performs as truncated cloak and concentrator, as predicted by our coordinate-transformation formalism. The mismatch between $\chi_{cc}$ and $\chi_{cc}^{sim}$ can be ascribed to the effect of the discretization of a continuous conducting medium which inevitably affects the overall voltage distribution in the MMEC. Another factor could be in the discrepancy of conductivity introduced by the silicon core area. However, the above results indicate that this difference does not sensibly alter the predicted MMEC performance.

### D. Measurements

The experimental characterization of the MMEC is carried out by mapping the voltage spatial distribution over the polar grid by probing the voltage at every node. The MMEC is fed with a 5 V dc power supply (HP 3611A) connected to the 19th node from the center of the polar grid [see Fig. 3(a)]. The voltage amplitude is measured with respect to the ground. A custom-made probe station with three motorized linear axes is used to sense the voltage at each node. Two stepper motors are programmed to position the sample horizontally, whereas a third stepper motor moves a spring-loaded contact probe vertically. The electric signal is measured with an HP34401A multimeter. In order to induce the desired change of the VO$_2$ resistivity, the sample was mounted on an electronically controlled hot chuck.

Figures 5(a) and 5(b) show the voltage maps measured at room temperature of $T = 22$ °C and at $T = 90$ °C, respectively. The region within the two red dashed circles is the tunable region. In Fig. 5(c), we also plot the VO$_2$ sheet resistance as a function of the temperature. The metal-insulator transition for the VO$_2$ used in this experiment was designed to take place between $T = 70$ °C and 75 °C. The measured voltage contour maps are markedly different at the two operating temperatures.
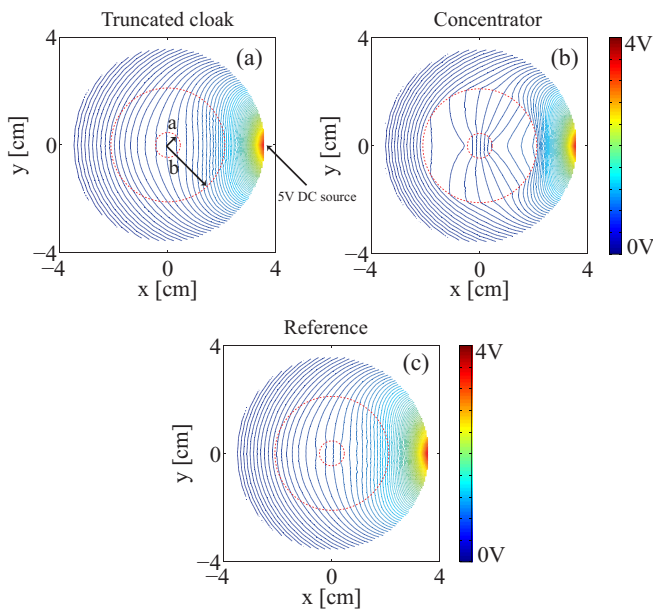


FIG. 4. (Color online) Numerically calculated voltage map for (a) the truncated cloak functionality, (b) the concentrator functionality, and (c) the reference. The source is placed to the right side, where the density of the equipotential lines is higher. The area enclosed between the red dashed circles is the tunable region.
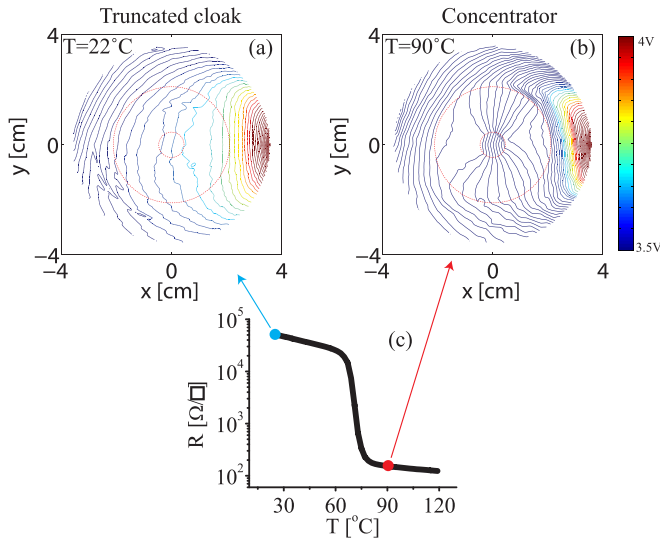
FIG. 5. (Color online) Contour map of the voltage levels measured at each node of the MMEC. (a) Voltage map for the truncated cloak functionality measured at $22\,°C$ and (b) voltage map for the concentrator functionality measured at $90\,°C$. (c) Experimentally measured sheet resistance curve of the $VO_2$ used in our experiment. Blue and red points show the sheet resistance values at 22 and $90\,°C$, respectively.

The voltage distribution at $T = 22\,°C$ refers to the case where the MMEC works as a truncated cloak. At $T = 90\,°C$, the profile changes drastically [see Fig. 5(b)] as a result of the $VO_2$ insulator-to-metal transition, and a voltage distribution characteristic of a concentrator (with equipotential lines pulled toward the core region) is observed. Under this condition, the $VO_2$ behaves as a conductor and the equivalent resistance of the radial branches is significantly lower. The experimentally measured map matches reasonably well the numerical simulations shown in Fig. 4. We point out that the natural $SiO_2$ thin film that grows on silicon when wafers are exposed to air prevented us from accurately measuring the voltage inside the core section. For this reason, the equipotential contour lines plotted in the core region are calculated by interpolating the voltage measured at the point outside the core.

### E. Discussion

The amplitude differences between the experimental and numerical contour maps are primarily caused by the conductivities of the TaN resistor matching network. For the sake of clarity, we have chosen two different lower ends (0 and 3.5 V for the simulation and experiments, respectively) in the color scales used to plot the contour maps in Figs. 4 and 5. TaN is deposited by means of sputtering, and its final conductivity is strongly dependent on the $N_2$ flow rate. We have found that this dependence is highly nonlinear, especially in proximity to the target values, thereby making it nontrivial to meet exactly the required values of the conductivities. Subsequent tests of the TaN resistivity values have confirmed a twofold difference with respect to the expected values. The present design is very demanding in terms of fabrication tolerances because the differences between the dimensions of neighboring resistors are small, ranging between 1 and 90 $\mu$m. For instance, typical

tolerances of the contact aligner $(+/-0.5\ \mu\text{m})$ could affect the above dimensions enough to cause noticeable fluctuations in the voltage profiles. This was made even more challenging as the MMEC required patterning of very small features with identical dimensions over a large surface. The irregular profile of some of the contour lines may be related to the nonuniformity of thin-film resistors across the entire 4-in. wafer. Despite the aforementioned fabrication matters, the experimental results show clear evidence of the ability of the MMEC to reconfigure its electric anisotropy.

A rigorous experimental characterization of the MMEC performance would require a comparison with a reference scenario. However, the issue of fabrication repeatability combined with the non-negligible fluctuations of manufacturing parameters prevented the fabrication of a reliable MMEC reference. For this reason, such comparison is restricted to numerical simulations only (see Sec. III C).

The experimental results reported in this paper suggest that the metamaterial paradigm may be used to provide solutions for tangible compact electronics using thin-film technologies. Traditionally, electronic systems comprise several blocks, each designed to play a specific role. A smarter design approach could rely on a single unit capable of handling multiple functions, such as carrying electric current and heat simultaneously but independently. A potential first step in this direction has been shown recently, by using metamaterial structures designed with the framework of multiphysics transformations [36]. The same goal may be approached through a different path of utilizing phase-change materials that have varying responses in different physical domains. For instance, it has been shown that $VO_2$ exhibits a change in its thermal conductivity upon phase transition, but it is dwarfed by the variation in its electrical conductivity [37–39]. This asymmetry in the two physical domains may be utilized to obtain two independent functionalities for heat and electricity. One can imagine adding right on top of a MMEC an additional network of material (such as $BeO_2$) with high thermal conductivity and limited electrical conductivity. When the metal-to-insulator transition takes place, only the electrical current profile within the overall material would be reconfigured, leaving the heat flux distribution unchanged. It is also conceivable to design layers to reconfigure both kinds of transport simultaneously but in different fashions. This line of bilayer approach, which takes advantage of nonlinear phase-change materials with strongly different electrical and thermal properties, may be useful for designing more compact electronic components with nontrivial multifunctionalities. In this connection, we note that a very interesting experimental work has recently been reported [26], in which thin-film technology combined with the coordinate-transformation approach is used to fabricate systems for the unconventional manipulation of heat flux using the discretization of thermal conductors to introduce anisotropy. Potential applications include thermal management of integrated circuits, e.g., capable of responding to temperature changes and rerouting the electrical current away from hot spots while reconfiguring its path in a prescribed and pseudoautomated fashion.

### IV. CONCLUSIONS

In conclusion, this work presents the development and characterization of a reconfigurable MMEC, designed to

respond to temperature changes through dynamic variation in its spatial anisotropy. The tunable MMEC device is fabricated by combining a network of thin-film resistors and vanadium dioxide (VO$_2$). The strong temperature dependence of the VO$_2$ electrical conductivity results in a significant modification of the resistor network behavior, giving rise to an additional level of functionalities. Through a set of coordinate-transformation equations, used to tailor the response of the MMEC upon temperature change, we have shown that our structure mimicking a continuous and anisotropic medium can act as a truncated cloak or a concentrator for electric currents. When designing an electronic system, the influence of the surrounding environment can be considered either a nuisance (and hence something to be suppressed) or a convenient knob that can be turned to affect the material properties. In the latter view, an ideal scenario would be to have the system designed in such a way that the external effect could be amplified and not only the local material characteristics but also the collective device property can be drastically manipulated with environmental stimuli. For such device designs and fabrications, a paradigm could appear from the combination of environmentally responsive (e.g., phase-change) materials and the framework of metamaterials tailored with the mathematical formalism of coordinate transformations.

## ACKNOWLEDGMENTS

## APPENDIX A: COORDINATE-TRANSFORMATION METHOD

We start by considering an auxiliary space $\mathbf{r}' \equiv (x',y',z')$ filled with an isotropic material with electrical conductivity $\sigma'$ [cf. Fig. 6(a)]. At equilibrium, the sourceless electrical conduction equation is given by

$$\nabla \cdot [\sigma'(\mathbf{r}')\nabla V'(\mathbf{r}')] = 0, \tag{A1}$$

with $V'$ denoting the electrical potential. Assuming, for instance, a homogeneous conductivity distribution $\sigma'$, and applying a constant voltage along a given direction, the electrical current density follows a straight path. Next, we
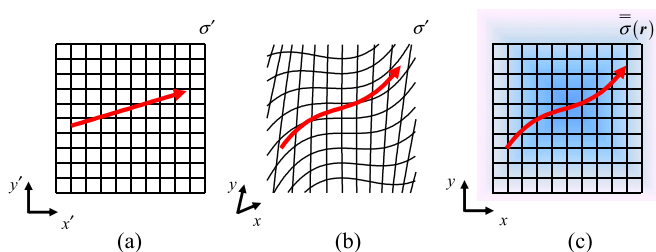


FIG. 6. (Color online) Path of the electric current density (red arrow) in (a) a Cartesian coordinate space filled with an isotropic material, (b) a transformed coordinate space filled with an isotropic material, and (c) a Cartesian coordinate space filled with inhomogeneous and anisotropic transformation medium with conductivity tensor $\bar{\bar{\sigma}}$.

apply a coordinate transformation

$$\mathbf{r}' = \mathbf{f}(\mathbf{r}) \tag{A2}$$

to a *curved-coordinate* space $\mathbf{r}$, which modifies the path of the electrical current density in a desired fashion [cf. Fig. 6(b)]. In view of the covariance properties of (A1), the transformation induced in the electric potential in this new space [20],

$$V(\mathbf{r}) = V'[\mathbf{f}(\mathbf{r})], \tag{A3}$$

can be equivalently obtained in a *flat* Cartesian space $\mathbf{r} \equiv (x,y,z)$ filled with an *inhomogeneous, anisotropic* "transformation medium" [cf. Fig. 6(c)] characterized by a conductivity tensor [20]

$$\bar{\bar{\sigma}}(\mathbf{r}) = \sigma' \det(\bar{\bar{\Lambda}})\bar{\bar{\Lambda}}^{-1} \cdot \bar{\bar{\Lambda}}^{-T}, \tag{A4}$$

where

$$\bar{\bar{\Lambda}} = \frac{\partial \mathbf{f}}{\partial \mathbf{r}} \tag{A5}$$

is the Jacobian matrix associated with the coordinate transformation in (A2), and the superscripts "−1" and "−T" denote the inverse and inverse transpose, respectively.

In particular, by considering a *radial* transformation

$$\rho' = f(\rho) \tag{A6}$$

between the associated cylindrical systems $(\rho',\phi',z')$ and $(\rho,\phi,z)$, the relevant components of the conductivity tensor in (A4) can be written as

$$\sigma_\rho(\rho) = \sigma' \frac{f(\rho)}{\rho \dot{f}(\rho)}, \quad \sigma_\phi(\rho) = \sigma' \frac{\rho \dot{f}(\rho)}{f(\rho)} \tag{A7}$$

with the overdot denoting differentiation with respect to the argument.

In our study, we are interested in switching between two functionalities induced by different coordinate transformations. More specifically, we consider an "invisibility-cloak" functionality induced by the coordinate transformation in (2), and a "concentrator" functionality induced by the coordinate transformation in (3). As illustrated in Fig. 7, for small values of $\delta$, the above cloak and concentrator transformations essentially map an annular cylinder of radii $a$ and $b > a$ in the transformed space $\mathbf{r}$ onto a cylinder of radius $b$ and an annular cylinder of radii $c > a$ and $b$, respectively, in the auxiliary space $\mathbf{r}'$. Figure 7 also illustrates the coordinate distortions induced by these two transformations.

We highlight that the transformations in (2) and (3) are *intertwined*, and they are slightly different from the ones
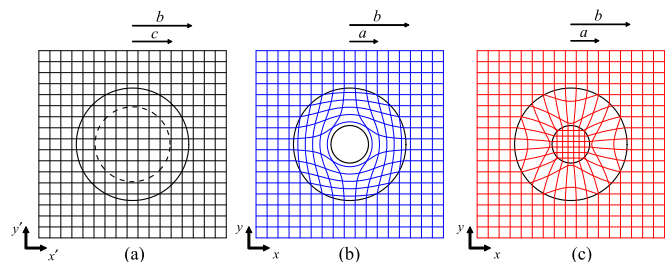


FIG. 7. (Color online) Schematic illustration of the coordinate transformations. (a) Auxiliary space; (b) and (c) transformed spaces for the cloak and concentrator transformations, respectively.

conventionally used in the literature [12,40]. In particular, the transformation in (2) actually yields an *imperfect* cloaking effect (with the ideal case recovered in the limit $\delta \rightarrow 0$), while the transformation in (3) is purposely chosen so as to simplify the subsequent implementation.

Via straightforward application of (A7), we can analytically derive the expressions of the conductivity profiles associated with the two transformations. More specifically, for the cloak functionality, we obtain

$$
\sigma_\rho^{\mathrm{ck}}(\rho) = \sigma'\left(\frac{\rho - a + \delta}{\rho}\right),
$$
$$
\sigma_\phi^{\mathrm{ck}}(\rho) = \sigma'\left(\frac{\rho}{\rho - a + \delta}\right),
$$
(A8)

from which we observe that the approximate character of the transformation in (2), for *finite* values of $\delta$, prevents the arising conductivity components from exhibiting *extreme* values at the inner boundary $\rho = a$, viz.,

$$
\sigma_\rho^{\mathrm{ck}}(a) = \frac{\sigma'\delta}{a}, \quad \sigma_\phi^{\mathrm{ck}}(a) = \frac{a}{\sigma'\delta}.
$$
(A9)

As a consequence, an *imperfect* cloaking effect is attained, with the electrical current density inside the inner region $\rho < a$ not exactly vanishing, but reduced by a factor $\chi_{\mathrm{ck}}$ in (5).

On the other hand, for the concentrator functionality, we obtain

$$
\sigma_\rho^{\mathrm{cc}}(\rho) = \frac{\sigma_\rho^{\mathrm{ck}}}{\gamma} = \sigma'\left(\frac{\rho - a + \delta}{\gamma\rho}\right),
$$
$$
\sigma_\phi^{\mathrm{cc}}(\rho) = \gamma\sigma_\phi^{\mathrm{ck}}(\rho) = \gamma\sigma'\left(\frac{\rho}{\rho - a + \delta}\right).
$$
(A10)

In this case, the electrical current density inside the inner region $\rho < a$ is enhanced by a factor $\chi_{\mathrm{cc}}$ in (6). The parameters $\delta$ and $\gamma$ can be computed from (5) and (6), once the desired cloaking and concentration factors $\chi_{\mathrm{ck}}$ and $\chi_{\mathrm{cc}}$, as well as the shell radii $a$ and $b$, have been set.

We note from (A9) and (A10) that the aforementioned *intertwining* of the two transformations yields, for the two functionalities, conductivity components that differ only by multiplicative constants. This significantly simplifies the subsequent implementation, based on a polar resistor network comprised of spokes and arcs of finite lengths $\Delta\rho$ and $\Delta\phi$, respectively, and thickness $t$. As shown in (1), the resistance profiles $R_\rho$ and $R_\phi$ in this network are readily related to the conductivity profiles via Ohm's law [12]. From (1), it is evident that the switching between the cloak and concentrator functionalities requires the reconfiguration of *both* resistance profiles $R_\rho$ and $R_\phi$. However, in our proposed design, we followed a simplified approach by assuming

$$
R_\phi^{\mathrm{ck}}(\rho) = R_\phi^{\mathrm{cc}}(\rho),
$$
(A11)

so that only the radial resistance profile $R_\rho$ needs to be reconfigured. In order to better understand the approximation underlying this assumption, it is insightful to look at the conductivity profiles generated by assuming that the cloak and concentrator transformations are applied to auxiliary spaces with different background conductivities $\sigma_{\mathrm{ck}}'$ and $\sigma_{\mathrm{cc}}'$,

respectively, viz.,

$$
\sigma_\rho^{\mathrm{ck}}(\rho) = \sigma_{\mathrm{ck}}'\left(\frac{\rho - a + \delta}{\rho}\right),
$$
$$
\sigma_\phi^{\mathrm{ck}}(\rho) = \sigma_{\mathrm{ck}}'\left(\frac{\rho}{\rho - a + \delta}\right),
$$
(A12)

$$
\sigma_\rho^{\mathrm{cc}}(\rho) = \sigma_{\mathrm{cc}}'\left(\frac{\rho - a + \delta}{\gamma\rho}\right),
$$
$$
\sigma_\phi^{\mathrm{cc}}(\rho) = \gamma\sigma_{\mathrm{cc}}'\left(\frac{\rho}{\rho - a + \delta}\right).
$$
(A13)

We note from (1) that the simplifying assumption in (A11) implies

$$
\sigma_\phi^{\mathrm{ck}}(\rho) = \sigma_\phi^{\mathrm{cc}}(\rho),
$$
(A14)

which can be achieved from (A13) by assuming

$$
\sigma_{\mathrm{ck}}' = \gamma\sigma_{\mathrm{cc}}',
$$
(A15)

and also yields

$$
\frac{R_\rho^{\mathrm{ck}}(\rho)}{R_\rho^{\mathrm{cc}}(\rho)} = \frac{\sigma_\rho^{\mathrm{cc}}(\rho)}{\sigma_\rho^{\mathrm{ck}}(\rho)} = \gamma^2.
$$
(A16)

We observe from (A16) that, in view of the judicious intertwining of the two transformations, the reconfiguration required on the radial resistance profile amounts only to a constant scaling factor.

The above interpretation, in terms of cloak and concentrator transformations applied to two different and properly chosen auxiliary spaces, inherently implies that it is no longer possible to achieve perfect impedance matching for both functionalities.

## APPENDIX B: PARAMETRIC STUDIES

In this Appendix, we present a numerical parametric study, showing the effects of the design parameters $\gamma$ and $\delta$ on the MMEC voltage distribution. For simplicity, numerical simulations are performed on a 2D model made of continuous elements. The conductivities of the core and the nontunable region are 10 and 600 S/m, respectively, whereas the tunable region is described by (A8) and (A10). As shown in (3), $\gamma$ influences only the current and voltage distribution when the MMEC operates as a concentrator. On the other hand, $\delta$ expresses the level of imperfection of a coordinate-transformation-based metamaterial cloak, when extreme parameters are not achievable. Figure 8 shows the contour plots of the voltage distribution for different values of $\gamma$ in the range $0 < \gamma < 1$, by assuming the same design parameters used in the experiment, $a = 3$ mm, $b = 21.5$ mm, and $\delta = 2$ mm. Numerical results clearly show that the ability to concentrate, as expressed by (6), weakens as $\gamma$ approaches 1. When the core region is significantly smaller than the tunable region, the difference $b - a$ has a strong effect on the ratio $\delta/(b - a + \delta)$ in (5) and (6). This, combined with a non-negligible value of $\delta$, results in $\delta/(b - a + \delta) \ll 1$, which leads to a strong dependence on small $\gamma$. On the other hand, the role played by the "imperfection" parameter $\delta$ is illustrated in Fig. 9, by assuming $\gamma = 0.672$. The parameter $\delta$ has a strong influence on the distribution of the equipotential lines around
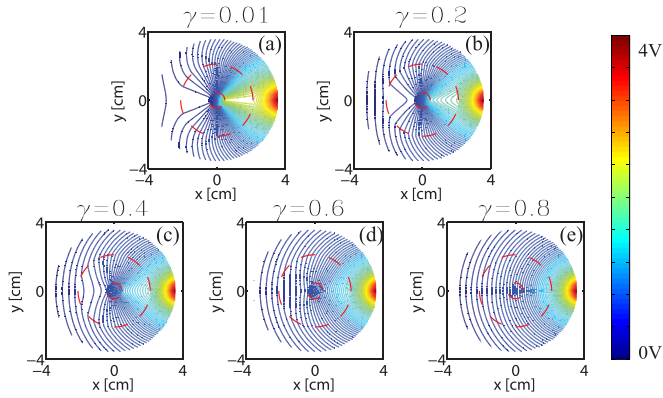
FIG. 8. (Color online) Numerical parametric analysis showing the MMEC voltage contour maps for different values of $\gamma$, calculated assuming $a = 3$ mm, $b = 21.5$ mm, and $\delta = 2$ mm.

the core region. Simulations show that large values of $\delta$ can have a detrimental effect on the overall voltage distribution and even change the nature of functionality that the device is designed to perform.

The results from the parametric study above have been exploited to find suitable sets of parameters that could enable an effective transition between the two functionalities. The final design is a compromise between reasonable values of $\chi_{\mathrm{ck}}$ and $\chi_{\mathrm{cc}}$. For a given $\chi_{\mathrm{ck}}$ the truncated-cloak functionality is strongly influenced by the radius $a$; the smaller $a$ the smaller the truncation parameter $\delta$. In order to avoid demanding fabrication solutions and to limit the spatial density of the radial and angular thin-film resistors in the vicinity of the MMEC center, we set $a = 3$ mm. This resulted in a value of $\delta$ which does not spoil the distribution of the equipotential line in the central region, as shown in Fig. 9(b). Subsequently, we chose a value of $\chi_{\mathrm{cc}}$ consistent with the overall change
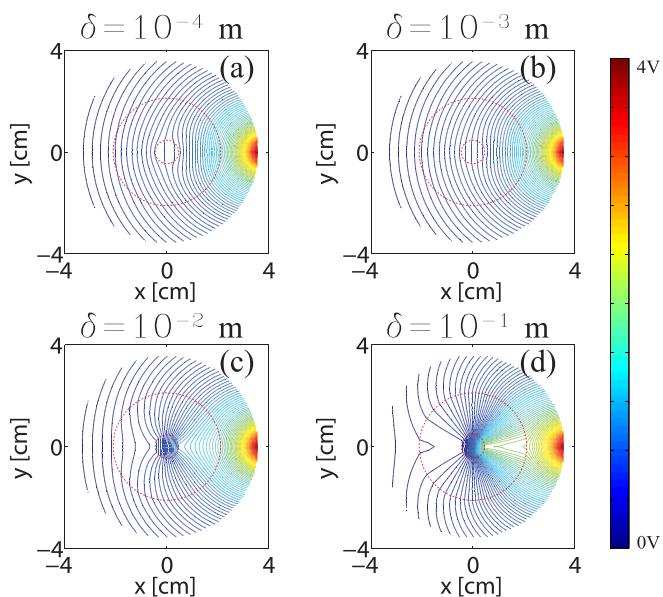


FIG. 9. (Color online) Numerical parametric analysis showing the MMEC voltage contour maps for different values of $\delta$, calculated assuming $a = 3$ mm, $b = 21.5$ mm, and $\gamma = 0.672$ mm.

in the resistance achievable with the parallel case of the two thin-film resistances made of VO$_2$ and Ti, respectively. The design proposed in the present work is not optimized, and there is room for further improvement.

## APPENDIX C: VO$_2$ DEPOSITION METHOD

VO$_2$ thin films were grown on 100-nm-thick thermal SiO$_2$ on Si wafer by rf magnetron sputtering from a V$_2$O$_5$ target in an Ar-O$_2$ gas mixture. The growth temperature and total pressure were kept constant at 550 °C and 5 mTorr during the deposition, respectively. It is known that the resistivity and the metal-insulator transition temperature of VO$_2$ are extremely sensitive to any subtle change in the oxygen partial pressure during the growth. As a result, the oxygen partial pressure was carefully controlled by adjusting the relative flow rate of pure Ar and that of 10% O$_2$ in Ar, which allows us to tune the oxygen partial pressure down to 0.02 mTorr when the total pressure is fixed at 5 mTorr. Figure 10 shows the resistivity-temperature curves of VO$_2$ samples grown under different oxygen partial pressure. The resistivity was measured by four-probe Van der Pauw measurements on a temperature-controlled hot chuck. The thickness of the films and therefore growth rate were calibrated by x-ray reflectivity and optical ellipsometry. The resistivity of VO$_2$ in both the insulating and metallic phases decreases with decreasing oxygen partial pressure, because of the extra free electrons donated by oxygen vacancies formed during the growth. When the oxygen partial pressure is zero, both the metal-insulator transition magnitude and temperature are suppressed by oxygen vacancy formation. On the other hand, if the oxygen partial pressure exceeds 0.1 mTorr, the deposited films are further oxidized into V$_2$O$_5$ that does not exhibit any metal-insulator transitions (not shown). As a result, in order to achieve a large on-off ratio and have reasonable device dimensions, for the present work we chose the resistivity-temperature curve of samples grown under oxygen partial pressure of 0.065 mTorr.
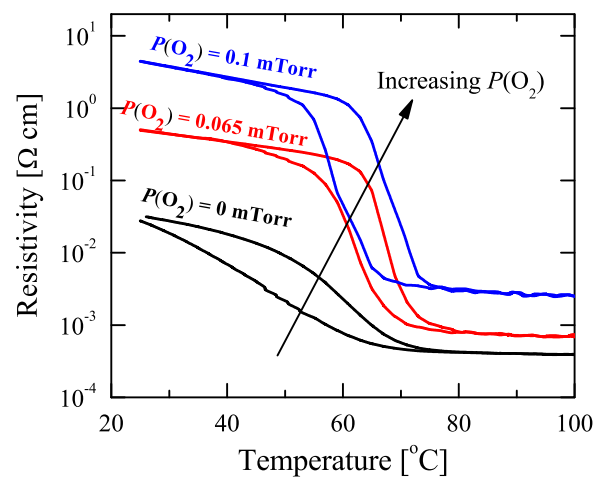


FIG. 10. (Color online) Plot of the resistivity measured for increasing levels of O$_2$ partial pressure. Experimental results were carried out on a 100-nm-thick VO$_2$ thin film.

TABLE I. (Left) Resistance values $R_\rho^{ck}$ and $R_\phi$ used to design the resistor network and the corresponding dimensions of the thin-film widths $w_\rho$ and $w_\phi$. They are sorted, through the index $n$, from closest to farthest from the center of the grid. (Right) Resistance values $R_m$ used to design the matching network and the corresponding dimensions of the thin-film widths $w_{R_m}$. They are sorted, through the index $n$, in terms of angular position starting from the element aligned with the source along the radial direction and moving counterclockwise.

| $n$ | $R_\rho^{ck}$ ($\Omega$) | $R_\phi$ ($\Omega$) | $w_\rho$ ($\mu$m) | $w_\phi$ ($\mu$m) | $n$ | $R_m$ ($\Omega$) | $w_{R_m}$ ($\mu$m) | $n$ | $R_m$ ($\Omega$) | $w_{R_m}$ ($\mu$m) |
|---|---|---|---|---|---|---|---|---|---|---|
| 1 | 39.26 | 3.79 | 217.93 | 228.11 | 1 | 100.30 | 2313.13 | 20 | 100.30 | 2313.13 |
| 2 | 33.75 | 8.80 | 253.47 | 314.72 | 2 | 1032.63 | 224.67 | 21 | 1032.63 | 224.67 |
| 3 | 31.77 | 13.99 | 269.31 | 334.11 | 3 | 1580.63 | 146.78 | 22 | 1580.63 | 146.78 |
| 4 | 30.73 | 19.28 | 278.36 | 341.17 | 4 | 1577.18 | 147.10 | 23 | 1577.18 | 147.10 |
| 5 | 30.10 | 24.61 | 284.19 | 344.70 | 5 | 1416.57 | 163.78 | 24 | 1416.57 | 163.78 |
| 6 | 29.68 | 29.93 | 288.24 | 347.11 | 6 | 1231.04 | 188.46 | 25 | 1231.04 | 188.46 |
| 7 | 29.37 | 35.29 | 291.24 | 348.38 | 7 | 1056.33 | 219.63 | 26 | 1056.33 | 219.63 |
| 8 | 29.14 | 40.66 | 293.55 | 349.25 | 8 | 900.91 | 257.52 | 27 | 900.91 | 257.52 |
| 9 | 28.96 | 46.00 | 295.36 | 350.11 | 9 | 765.49 | 303.08 | 28 | 765.49 | 303.08 |
| 10 | 28.82 | 51.37 | 296.85 | 350.56 | 10 | 648.67 | 357.66 | 29 | 648.67 | 357.66 |
| 11 | 27.50 | 59.24 | 311.09 | 336.19 | 11 | 548.68 | 422.84 | 30 | 548.68 | 422.84 |
| 12 | 27.50 | 64.62 | 311.09 | 337.67 | 12 | 463.85 | 500.16 | 31 | 463.85 | 500.16 |
| 13 | 27.50 | 70.00 | 311.09 | 338.92 | 13 | 392.78 | 590.66 | 32 | 392.78 | 590.66 |
| 14 | 27.50 | 75.38 | 311.09 | 340.00 | 14 | 334.34 | 693.90 | 33 | 334.34 | 693.90 |
| 15 | 27.50 | 80.76 | 311.09 | 340.93 | 15 | 287.63 | 806.59 | 34 | 287.63 | 806.59 |
| 16 | 27.50 | 86.14 | 311.09 | 341.75 | 16 | 251.96 | 920.78 | 35 | 251.96 | 920.78 |
| 17 | 27.50 | 91.53 | 311.09 | 342.47 | 17 | 226.83 | 1022.81 | 36 | 226.83 | 1022.81 |
| 18 | 27.50 | 96.91 | 311.09 | 343.11 | 18 | 211.88 | 1094.97 | 37 | 211.88 | 1094.97 |
| 19 | 27.50 | 102.29 | 311.09 | 343.68 | 19 | 206.92 | 1121.22 | | | |

## APPENDIX D: DEVICE PARAMETERS

The MMEC design is comprised of two steps. During the first step, we calculate the resistance values $R_\rho$ and $R_\phi$ from (1). To validate our design, we run numerical simulations of the polar grid network using COMSOL MULTIPHYSICS [35]. For the device fabricated experimentally with thin-film technologies, different resistance values are achieved by using materials of fixed conductivities but varying the dimensions of relevant spokes and arcs making up the discretized grid. For numerical simulations, to simplify the computation, spokes and arcs of fixed dimensions are used while varying

their electrical conductivities in order to match the desired anisotropic profile obtained from (1). The second design step involves the calculation of the dimensions of the polar grid for the real device. Table I lists the values of $R_\rho^{ck}$ and $R_\phi$ of the thin-film resistors used in our experiment and the value of the corresponding widths. Lengths and angular dimensions are fixed to $\Delta\rho = 1850\ \mu$m and $\Delta\phi = 10°$, respectively. Resistors have been fabricated with Ti films ($\rho_{Ti} = 132\ \mu\Omega$ cm) and the film thickness is fixed at $t_{Ti} = 200$ nm.

Also listed in Table I are the resistances $R_m$ and widths $w_{Rm}$ of the matching network. Referring to Fig. 11 for illustration of the parameters, the values are derived from

$$R_m = \frac{d(\ln r_0 - \ln d)}{\sigma_0 R_0 \Delta\phi h \cos\beta} \tag{D1}$$

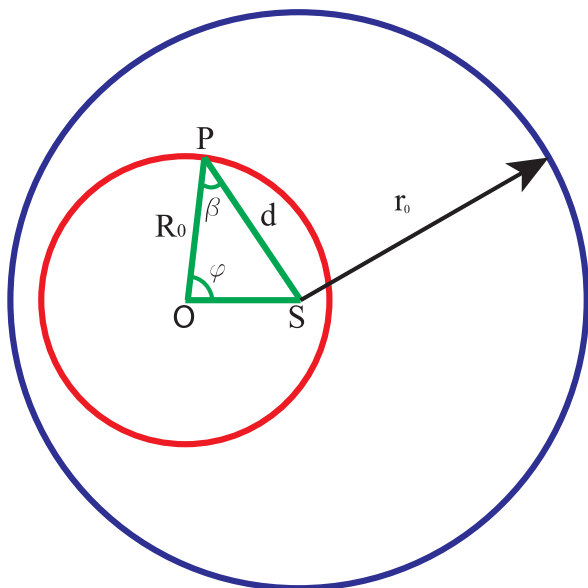to emulate an infinite medium [12]. In particular, $r_0$ is the distance between the ground and the source point $S$, $\sigma_0$ is the



FIG. 11. (Color online) Schematic showing the geometrical parameters used for the derivation of the matching resistor network.

TABLE II. Resistance values $R_{VO_2}^{insul}$ and $R_{VO_2}^{cond}$ used to design the VO$_2$ resistors and the corresponding dimensions of the thin-film widths $w_{VO_2}$. They are sorted, through the index $n$, from closest to farthest to the center of the grid.

| $n$ | $R_{VO_2}^{insul}$ ($\Omega$) | $R_{VO_2}^{cond}$ ($\Omega$) | $w_{VO_2}$ ($\mu$m) |
|---|---|---|---|
| 1 | 715.29 | 2.15 | 1615.23 |
| 2 | 614.99 | 1.85 | 1878.64 |
| 3 | 578.81 | 1.74 | 1996.10 |
| 4 | 559.99 | 1.69 | 2063.18 |
| 5 | 548.50 | 1.65 | 2106.38 |
| 6 | 540.80 | 1.63 | 2136.37 |
| 7 | 535.23 | 1.61 | 2158.63 |
| 8 | 531.02 | 1.60 | 2175.71 |
| 9 | 527.76 | 1.59 | 2189.18 |
| 10 | 525.12 | 1.58 | 2200.17 |

conductivity of the background medium ($\sigma_0 = 600$ S/m), $h = 0.5$ mm, and $\Delta\phi = 10°$. The $R_m$ resistors are made with TaN ($\rho_{\mathrm{TaN}} = 2280$ $\mu\Omega$ cm). The $w_{Rm}$ values are calculated through Ohm's law where we fix the radial length ($\Delta\rho = 1850$ $\mu$m) and the thickness ($t_{\mathrm{TaN}} = 200$ nm).

Table II lists the resistance values $R_{\mathrm{VO_2}}^{\mathrm{insul}}$ and $R_{\mathrm{VO_2}}^{\mathrm{cond}}$ in the insulating ($T = 22\,°\mathrm{C}$) and conductive ($T = 90\,°\mathrm{C}$) states.

Through Ohm's law, we calculate the corresponding widths of the resistors $w_{\mathrm{VO_2}}$. Also for these VO$_2$ resistors we have fixed the lengths $l_{\mathrm{VO_2}} = 15$ $\mu$m) and thicknesses ($t_{\mathrm{VO_2}} = 300$ nm). In our numerical simulations, the conductivity of the core region was properly scaled so as to account for the difference in thickness between the silicon layer and the thin films forming the polar grid.

---

[1] M. Kadic, T. Bückmann, R. Schittny, and M. Wegener, Rep. Prog. Phys. **76**, 126501 (2013).

[2] M. Maldovan, Nature (London) **503**, 209 (2013).

[3] L. Zigoneanu, B.-I. Popa, and S. A. Cummer, Nat. Mater. **13**, 352 (2014).

[4] B.-I. Popa, L. Zigoneanu, and S. A. Cummer, Phys. Rev. Lett. **106**, 253901 (2011).

[5] H. Chen, C. Chan, and P. Sheng, Nat. Mater. **9**, 387 (2010).

[6] S. Narayana and Y. Sato, Adv. Mater. **24**, 71 (2012).

[7] F. Magnus, B. Wood, J. Moore, K. Morrison, G. Perkins, J. Fyson, M. Wiltshire, D. Caplin, L. Cohen, and J. Pendry, Nat. Mater. **7**, 295 (2008).

[8] F. Gömöry, M. Solovyov, J. Šouc, C. Navau, J. Prat-Camps, and A. Sanchez, Science **335**, 1466 (2012).

[9] S. Narayana and Y. Sato, Phys. Rev. Lett. **108**, 214303 (2012).

[10] S. Narayana, S. Savo, and Y. Sato, Appl. Phys. Lett. **102**, 201904 (2013).

[11] R. Schittny, M. Kadic, S. Guenneau, and M. Wegener, Phys. Rev. Lett. **110**, 195901 (2013).

[12] F. Yang, Z. L. Mei, T. Y. Jin, and T. J. Cui, Phys. Rev. Lett. **109**, 053902 (2012).

[13] N. Papasimakis, Z. Luo, Z. X. Shen, F. De Angelis, E. Di Fabrizio, A. E. Nikolaenko, and N. I. Zheludev, Opt. Express **18**, 8353 (2010).

[14] Z. Samson, K. MacDonald, F. De Angelis, B. Gholipour, K. Knight, C. Huang, E. Di Fabrizio, D. Hewak, and N. Zheludev, Appl. Phys. Lett. **96**, 143105 (2010).

[15] S. Savo, D. Shrekenhamer, and W. J. Padilla, Adv. Opt. Mater. **2**, 275 (2014).

[16] J.-Y. Ou, E. Plum, L. Jiang, and N. I. Zheludev, Nano Lett. **11**, 2142 (2011).

[17] V. Savinov, V. Fedotov, S. Anlage, P. De Groot, and N. Zheludev, Phys. Rev. Lett. **109**, 243904 (2012).

[18] T. Driscoll, H.-T. Kim, B.-G. Chae, B.-J. Kim, Y.-W. Lee, N. M. Jokerst, S. Palit, D. R. Smith, M. Di Ventra, and D. N. Basov, Science **325**, 1518 (2009).

[19] W. X. Huang, X. G. Yin, C. P. Huang, Q. J. Wang, T. F. Miao, and Y. Y. Zhu, Appl. Phys. Lett. **96**, 261908 (2010).

[20] J. B. Pendry, D. Schurig, and D. R. Smith, Science **312**, 1780 (2006).

[21] W. X. Jiang, C. Y. Luo, H. F. Ma, Z. L. Mei, and T. J. Cui, Sci. Rep. **2**, 956 (2012).

[22] W. X. Jiang, C. Y. Luo, Z. L. Mei, and T. J. Cui, Appl. Phys. Lett. **102**, 014102 (2013).

[23] Q. Ma, Z. L. Mei, S. K. Zhu, T. Y. Jin, and T. J. Cui, Phys. Rev. Lett. **111**, 173901 (2013).

[24] D. Schurig, J. J. Mock, B. J. Justice, S. A. Cummer, J. B. Pendry, A. F. Starr, and D. R. Smith, Science **314**, 977 (2006).

[25] U. Leonhardt, Science **312**, 1777 (2006).

[26] E. M. Dede, T. Nomura, P. Schmalenberg, and J. S. Lee, Appl. Phys. Lett. **103**, 063501 (2013).

[27] O. J. Zobel, Bell Syst. Tech. J. **2**, 1 (1923).

[28] E. Norton, Bell Syst. Tech. J. **16**, 178 (1937).

[29] Y. Han, O. Leitermann, D. A. Jackson, J. M. Rivas, and D. J. Perreault, IEEE Trans. Power Electron. **22**, 41 (2007).

[30] L. Borcea, V. Druskin, and F. G. Vasquez, Inverse Probl. **24**, 035013 (2008).

[31] M. Cheney, D. Isaacson, and J. C. Newell, SIAM Rev. **41**, 85 (1999).

[32] C. Roos, Y. Bai, and D. Chaerani, SQU J. Sci. **17**, 125 (2012).

[33] D. J. Klein and M. Randić, J. Math. Chem. **12**, 81 (1993).

[34] Z. Ruan, M. Yan, C. W. Neff, and M. Qiu, Phys. Rev. Lett. **99**, 113903 (2007).

[35] Multiphysics Reference Guide for COMSOL 4.2 (COMSOL, Burlington, MA, 2011).

[36] M. Moccia, G. Castaldi, S. Savo, Y. Sato, and V. Galdi, Phys. Rev. X **4**, 021025 (2014).

[37] V. Andreev, F. Chudnovskii, A. Petrov, and E. Terukov, Phys. Status Solidi A **48**, K153 (1978).

[38] J. Chen, X. Liu, X. Yuan, Y. Zhang, Y. Gao, Y. Zhou, R. Liu, L. Chen, and N. Chen, Chin. Sci. Bull. **57**, 3393 (2012).

[39] D. W. Oh, C. Ko, S. Ramanathan, and D. G. Cahill, Appl. Phys. Lett. **96**, 151906 (2010).

[40] M. Rahm, D. Schurig, D. A. Roberts, S. A. Cummer, D. R. Smith, and J. B. Pendry, Photon. Nano. Fund. Appl. **6**, 87 (2008).